

PROCEEDINGS OF SPIE

[SPIDigitalLibrary.org/conference-proceedings-of-spie](https://spiedigitallibrary.org/conference-proceedings-of-spie)

Optimization of a dual wavelength atlas technique to differentiate methylene blue from hemoglobin in photoacoustic signals

Gonzalez, Eduardo, Graham, Camryn, Lediju Bell, Muyinatu

Eduardo A. Gonzalez, Camryn A. Graham, Muyinatu A. Lediju Bell, "Optimization of a dual wavelength atlas technique to differentiate methylene blue from hemoglobin in photoacoustic signals," Proc. SPIE 11960, Photons Plus Ultrasound: Imaging and Sensing 2022, 119600A (3 March 2022); doi: 10.1117/12.2607825

SPIE.

Event: SPIE BiOS, 2022, San Francisco, California, United States

Optimization of a Dual Wavelength Atlas Technique to Differentiate Methylene Blue from Hemoglobin in Photoacoustic Signals

Eduardo A. Gonzalez^a, Camryn A. Graham^b, and Muyinatu A. Lediju Bell^{a,c,d}

^aDepartment of Biomedical Engineering, Johns Hopkins University, Baltimore, MD, USA

^bDepartment of Biomedical Engineering, University of Michigan, Ann Arbor, MI, USA

^cDepartment of Electrical and Computer Engineering, Johns Hopkins University, Baltimore, MD, USA

^dDepartment of Computer Science, Johns Hopkins University, Baltimore, MD, USA

ABSTRACT

In photoacoustic-guided surgery, it is important to differentiate between critical structures that provide photoacoustic contrast. We developed a novel dual-wavelength atlas method to differentiate between two chromophores using only two optical wavelengths. In this work, we report our methods to optimize this approach by varying six parameters: absolute value, modulation frequency, filter bandwidth, kernel size, number of principal components, and number of nearest neighbor classifiers. Sensitivity, specificity, and balanced accuracy were the three metrics used to determine the optimal value for each parameter. An iterative process was used to determine the optimal set of parameters by changing each parameter one at a time and finding which value returned the highest combination of sensitivity and specificity. The optimal parameters included using the non-absolute value of the radiofrequency signals, a modulation frequency of 1 MHz, a bandwidth of 140%, a kernel size of 60 pixels, 1 principal component, and 1 nearest neighbor classifier. These parameters improved the mean \pm one standard deviation of balanced accuracy from 0.78 ± 0.12 to 0.88 ± 0.16 in the dual wavelength atlas method. The speed of delivering this algorithm was further optimized by implementing a GPU coherence beamforming approach to selecting regions of interest for the frequency analysis. These results are promising for surgeons using contrast agents during photoacoustic-guided surgery.

1. INTRODUCTION

Differentiation of tissues and biomarkers is anticipated to be an essential component of complex photoacoustic-guided surgery approaches to visualize surgical tools and avoid major blood vessels, nerves, and other critical structures.¹⁻³ Spectral unmixing techniques may be employed to differentiate photoacoustic responses originating from these structures.⁴⁻⁸ These techniques consist of generating an overdetermined system of equations (i.e., more equations than variables) from the signal response of each chromophore at different laser wavelengths, which can then be solved with an optimization technique based on the known optical absorption coefficient for each chromophore at each wavelength.^{9,10} Despite their effectiveness, these spectral unmixing techniques are less desirable for real-time applications because of the lengthy acquisition time requirements associated with transmitting multiple laser wavelengths.

To overcome the challenges of spectral unmixing, we recently developed a dual-wavelength acoustic-frequency-based atlas method.^{11,12} This method considers differences in acoustic frequency spectra and provides information for differentiation among photoacoustic biomarkers for surgical guidance (e.g., contrast agents, blood vessels). By using coherence imaging¹³ to segment photoacoustic signals of interest, the dual-wavelength atlas method differentiates surgical biomarkers using only two optical wavelengths, which is highly desirable for surgical guidance. This method was initially reported with a mean balanced accuracy of 78% when differentiating between methylene blue and blood.¹¹ In addition, the translation of the current method to real-time applications is limited by the high processing times of the coherence mask used to identify regions of interest for analysis. Computation times can potentially be reduced by generating masks from graphical processing

unit (GPU)-based short-lag spatial coherence (SLSC) images,¹⁴ rather than the previous central processing unit (CPU)-based coherence approach.¹³

This paper presents our approach to optimization of the novel dual-wavelength atlas method for the differentiation of an exogenous chromophore (i.e., methylene blue) and an endogenous chromophore (i.e., human blood) by varying six parameters utilized in the extraction and classification steps (i.e. absolute value, modulation frequency, filter bandwidth, kernel size, number of principal components, and number of nearest neighbor classifiers). Balanced accuracy was the primary optimization metric and an iterative process was used to determine the optimal set of parameters by changing each parameter one at a time. Finally, the reduction of processing times for the dual-wavelength atlas method was explored when segmenting the signals of interest with GPU-SLSC beamforming instead of the previous CPU-based coherence beamforming.¹³

2. METHOD

2.1 Data acquisition

Photoacoustic signals from methylene blue (MB) and human blood (Hb) were acquired from a phantom setup.¹¹ A polyvinyl chloride-plastisol (PVCPI) was fabricated with length, width, and height of 29 cm, 18 cm, and 10 cm, respectively. The phantom contained ten cylindrical hollow chambers. Each of these chambers had a diameter of 15 mm and a depth of 55 mm. Two of the hollow chambers were filled with a 1% weight-by-volume aqueous solution of MB and Hb, and a 1-mm-diameter optical fiber was inserted in each of the filled chambers. These fibers originated from a bifurcated fiber bundle that was connected to a Phocus Mobile laser (Opotek Inc., Carlsbad, CA, USA), transmitting laser light with wavelengths ranging 690-950 nm in 10 nm increments. The tip of each optical fiber was positioned approximately 15 mm below the top surface of the chambers, and photoacoustic signals were generated with an energy of 4 mJ at each fiber tip. The generated photoacoustic signals were received by an Alpinion L3-8 linear array ultrasound probe that was positioned on the lateral wall of the phantom, as described in our previous publication.¹¹

2.2 Dual-wavelength atlas method

Fig. 1 shows an overview of the dual-wavelength atlas method. First, ground-truth labels of MB and Hb were segmented from locally weighted short-lag spatial coherence (LW-SLSC) images,^{13,15} using a regularization factor

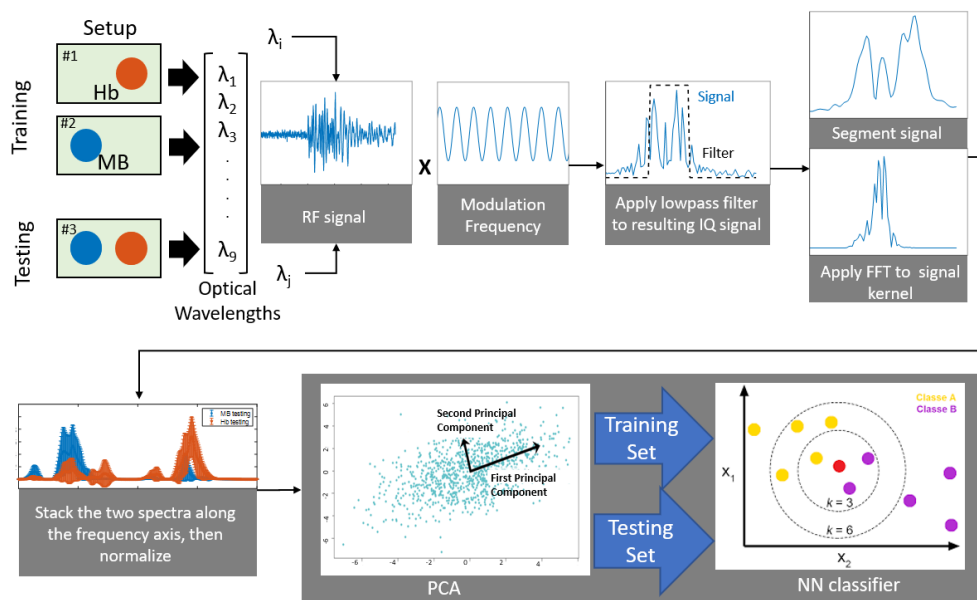


Figure 1: Pipeline of the dual-wavelength atlas method

of $\alpha = 1$ and an axial correlation kernel of 2λ , where λ is the wavelength associated with the center frequency of the L3-8 ultrasound probe. Binary segmentation was performed using a -6 dB threshold mask applied to the LW-SLSC images. A frequency analysis was performed over the magnitude of the pressure waves, which were either zero or positive, rather than the original pressure waves used for conventional beamforming, which have positive and negative values. For each material (i.e., MB and Hb), the normalized power spectra were calculated from a sliding window of axial kernels of in-phase and quadrature (IQ) data. Then, principal component analysis (PCA) was applied to the power spectra of photoacoustic signals acquired at each laser wavelength. The principal components were stored in an “atlas” describing each material. Finally, when evaluating the spectra of a test signal, nearest neighbor (k-NN) classification was applied with the L2-norm as the measure of distance between the PCA of the test spectra and the PCA of the spectra within the atlas.

2.3 Image quality metrics

MB and Hb were considered to be the positive and negative samples, respectively, when calculating sensitivity, specificity, and balanced accuracy metrics of the classification performance. The formula for each of these metrics are given by:

$$\text{Sensitivity} = \frac{T_{MB}}{T_{MB} + F_{Hb}}, \quad (1)$$

$$\text{Specificity} = \frac{T_{Hb}}{T_{Hb} + F_{MB}}, \quad (2)$$

$$\text{Balanced Accuracy} = \frac{\text{Sensitivity} + \text{Specificity}}{2}, \quad (3)$$

where T_{MB} , T_{Hb} , F_{MB} , and F_{Hb} are the number of true MB, true Hb, false MB, and false Hb pixels, respectively.


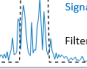

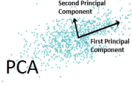
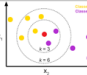
2.4 Parameter optimization

To maximize the balanced accuracy of our approach (see Eq. 3), the parameters for in-phase quadrature demodulation, PCA, and NN were optimized through an iterative search. These parameters were the modulation frequency, filtered bandwidth, axial kernel size, number of principal components to use, and the k nearest neighbors used to determine the most common class in k-NN clustering. During each analysis, the optimal parameter found from the previous step was saved and used to find the new output until the optimal set of parameters were found. For the IQ-modulation, different combinations of bandwidth of 80-240% in intervals of 20% were tested with the modulation frequency varied from 2 MHz to 12 MHz in intervals of 2 MHz. Similarly, the axial kernel size was explored from 11 to 51 axial samples in increments of 2. For the PCA, the principal components were varied from 10 to 200 in steps of 10 and then from 1-10 in steps of 1. Finally, the NN classifier was analyzed by changing the classifier to 2-NN through 10-NN in increments of 1. The initial parameters were obtained from a previous publication in our group.¹¹ To speed up the optimization process, the iterations were conducted on a reduced dataset obtained with laser wavelengths ranging from 690 nm to 950 nm in 30 nm increments. Table 1 shows the parameters considered for optimization, their initial value, and the optimized value that achieved the highest balanced accuracy for differentiating MB and Hb.

2.5 Optimization of processing times

To reduce the computational time consumed by LW-SLSC beamforming, the performance of the optimized dual-wavelength atlas method was explored with testing data obtained from GPU-SLSC masks. First, the parameters of the GPU-SLSC beamforming and the binary threshold were adjusted in order to achieve the closest match to the original LW-SLSC masks. Cumulative lag sum M and axial wavelength λ were varied from 1 to 10 in steps of one and from 1 to 4 in steps of 0.2, respectively, and the binary threshold to generate the masks was set to 0.7. Then, the Dice coefficient (DSC)¹⁶ was used as a metric to maximize the similarity between GPU-SLSC masks and the original LW-SLSC masks. After finding the optimal pair of M and λ , the optimal threshold for binary segmentation was found by varying the binary threshold from 0.1 to 0.98 in steps of 0.02 and using the DSC to maximize the similarity between generated masks. Computation times were estimated for 1 frame of each wavelength for both LW-SLSC and GPU-SLSC masks. The LW-SLSC and GPU-SLSC algorithms

Table 1: Summary of optimized parameters for the dual-wavelength atlas method

| Parameter | Purpose | Illustration | Initial Value | Range Tested | Increment Size | Optimal Value |
|-----------------------------|---|---|---------------|----------------|----------------|---------------|
| Absolute Value | Takes magnitude of RF signal | - | Yes | - | - | None |
| Modulation Frequency | Converts RF signals to IQ signals |  | 5 MHz | 2-12 MHz | 1 MHz | 2.0 MHz |
| Bandwidth | Determine the cut-off frequency of the lowpass filter |  | 300% | 80-240% | 20% | 140% |
| Kernel Size | Influences FFT resolution |  | 40 pixels | 22-102 pixels | 2 pixels | 60 pixels |
| Principal Components | Describes number of orthogonal linear coordinates that data can represent |  | 50 | 1-10 10-200 | 1 10 | 1 |
| Nearest Neighbor Classifier | Classifier represents distance to the closest match in the atlas |  | 1st | 1-10 | 1 | 1st |

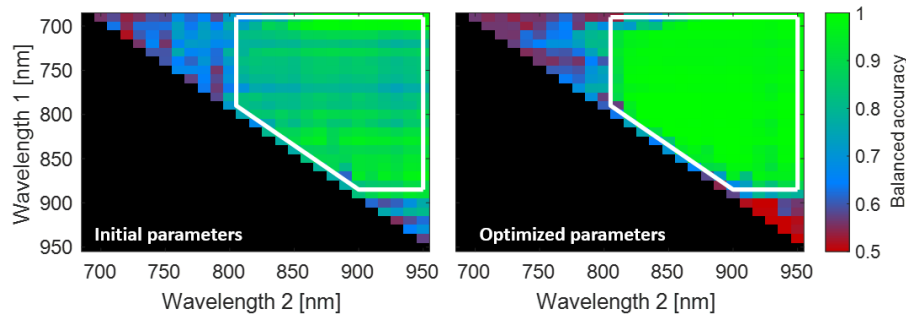
were executed with an Intel Core i5-6600K CPU and a NVIDIA Titan Xp GPU, respectively, both of the devices installed on the same computer. Finally, the statistical significance of performance differences between LW-SLSC and GPU-SLSC was evaluated with a Mann-Whitney U test.¹⁷

3. RESULTS

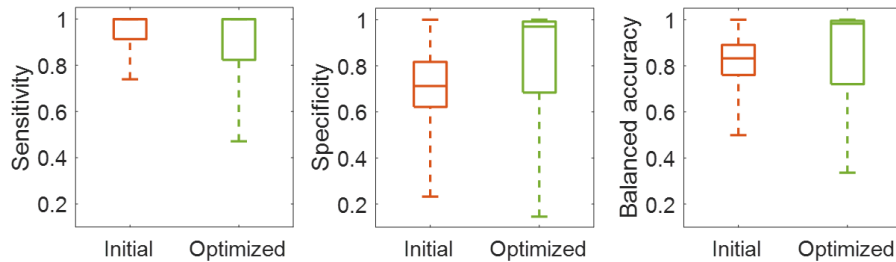
Fig. 2 shows the classification results achieved before and after parameter optimization. The mean balanced accuracy of classification results for the dual-wavelength atlas method are displayed in Fig. 2(a). Each pixel displays the average accuracy of classifying methylene blue and blood for a specific wavelength pair over 10 frames, with redundancies of wavelength pair information represented as black pixels in the bottom left half of each image. Although 36 wavelength pairs were used for the optimization process, this result shows the balanced accuracy for a total of 351 wavelength pair combinations. For wavelength pairs located in the mid-wavelength region (outlined in white), the mean \pm one standard deviation of balanced accuracy increased from $86.2 \pm 7.2\%$ with the initial parameters reported in Table 1 to $96.7 \pm 7.7\%$ when using optimized parameters. In contrast, for wavelength pairs located outside the mid-wavelength region, the balanced accuracy decreased from $74.67 \pm 8.3\%$ to $67.40 \pm 8.9\%$. The number of wavelength pairs residing above a pre-defined balanced accuracy threshold of 95% increased from 25 wavelength pairs with the initial parameters to 217 with the optimized parameters. This increase of wavelength pairs leads to an increase in available options for differentiating methylene blue from hemoglobin. Fig. 2(b) shows a summary of the sensitivity, specificity, and balanced accuracy for all of the wavelength pairs investigated before and after optimization. The mean \pm one standard deviation of sensitivity showed no significant change from $91.6 \pm 16.8\%$ to $90.9 \pm 14.8\%$. However, an increase in specificity was observed from $70.7 \pm 16.9\%$ to $81.7 \pm 20.9\%$, which in turn resulted in an overall increase of specificity from $81.5 \pm 10.4\%$ to $85.9 \pm 17.1\%$.

Fig. 3 shows the process of finding the parameters that generated GPU-SLSC masks most similar to the LW-SLSC masks. Fig. 3(a) shows the mean DSC from 27 laser wavelength emission obtained when comparing the original LW-SLSC masks with GPU-SLSC from different combinations of M and λ and a coherence threshold of 0.7. Fig. 3(b) shows the DSC obtained when comparing the original LW-SLSC masks with GPU-SLSC masks generated from $M = 5$, $\lambda = 4$, and varying the coherence threshold for binary segmentation. The GPU-SLSC masks generated with $M = 5$, $\lambda = 4$, and a coherence threshold of 0.75 was the most similar to LW-SLSC masks with a mean \pm one standard deviation DSC of $63.3\% \pm 4.2\%$.

Fig. 4 shows the classification results achieved when switching between LW-SLSC masks and the similar GPU-SLSC masks. The mean balanced accuracy for 36 wavelength pairs when using LW-SLSC and GPU-SLSC masks is shown in Fig. 4(a). A comparative summary of the sensitivity, specificity, and balanced accuracy for

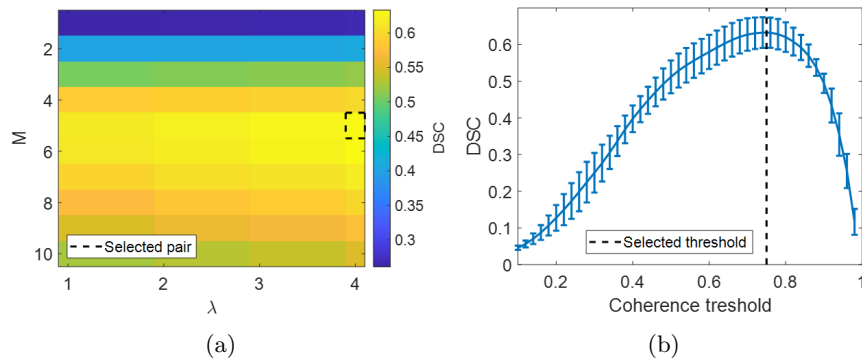


(a)



(b)

Figure 2: Classification performance results of the dual-wavelength atlas method before and after parameter optimization. (a) Mean balanced accuracy across 10 frames for each wavelength pair. (b) Comparison of sensitivity, specificity, and balanced accuracy obtained from Mask 1, 2, and 3.



(a)

(b)

Figure 3: Comparison of LW-SLSC masks with GPU-SLSC masks using the Dice coefficient (DSC). (a) Mean DSC (from 27 wavelengths) obtained when comparing the original LW-SLSC masks with GPU-SLSC masks generated from different combinations of M and λ and a coherence threshold of 0.7. (b) DSC obtained when comparing the original LW-SLSC masks with GPU-SLSC masks generated from $M = 5$, $\lambda = 4$, and varying the coherence threshold for binary segmentation. Each error bar is generated from measurements of 27 wavelengths. The highest mean DSC is represented by the dotted box and dotted line for (a) and (b), respectively.

the different masks is shown in Fig. 4(b). The mean \pm one standard deviation of sensitivity for LW-SLSC and GPU-SLSC was $91.0 \pm 17.6\%$ and $90.6 \pm 17.7\%$, respectively, representing a minimal differences between the two approaches. In contrast, the specificity increased from $83.9 \pm 24.1\%$ to $86.5 \pm 22.5\%$ when switching from LW-SLSC to GPU-SLSC masks. This increase in specificity resulted in an increase of balanced accuracy from $87.4 \pm 18.2\%$ to $89.2 \pm 16.9\%$ for LW-SLSC and GPU-SLSC, respectively. However, the difference of balanced accuracy was not statistically significant ($p > 0.001$). Finally, a summary of computation times for a single frame are shown in Fig. 4(c), where the GPU-SLSC achieved a speed up factor of approximately 60.2x. Each box plot

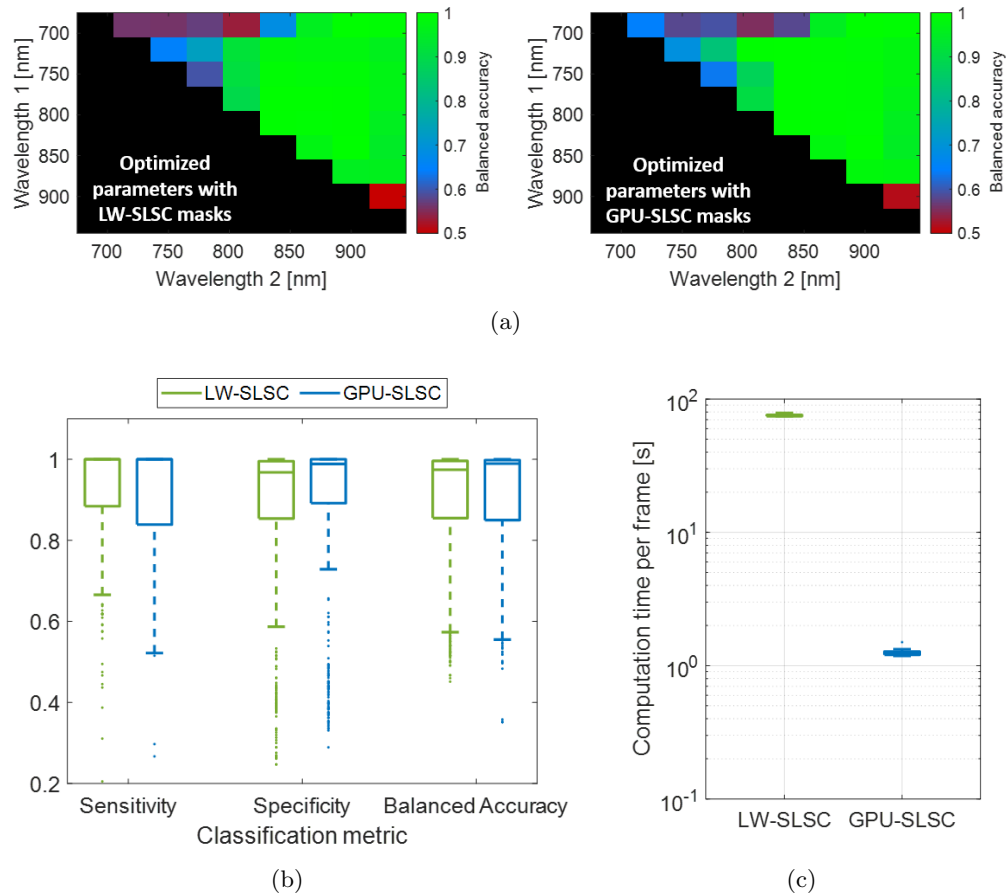


Figure 4: Classification performance results of the dual-wavelength atlas method with optimized parameters tested on data extracted from different coherence masks. (a) Mean balanced accuracy across 10 frames for each masks and wavelength pair. (b) Comparison of sensitivity, specificity, and balanced accuracy obtained from LW-SLSC and GPU-SLSC masks. (c) Comparison of processing times for a single photoacoustic frame using LW-SLSC and GPU-SLSC.

represents the computation times from a total of 27 frames (i.e., one frame per laser emission wavelength). In addition, the difference between computation times achieved with GPU-SLSC and LW-SLSC was statistically significant ($p < 0.001$).

4. DISCUSSION

The increased specificity with the optimized parameters for the dual wavelength method demonstrates an increased capacity for the algorithm to differentiate blood from methylene blue, as blood was considered as negative sample for the specificity metric (see Section 2.3). Similarly, the higher balanced accuracy with more wavelength pairs leads to an increase in available options for differentiating methylene blue from hemoglobin. This is particularly important during image-guided surgeries, where additional chromophores are present and their photoacoustic response can interfere with the classification algorithm for a specific wavelength pair. To avoid this interference, a surgeon might switch to a different wavelength-pair emission with similar classification performance between Hb and MB.

Regarding the decreased mean balanced accuracy observed in Fig. 2(a) for wavelength pairs outside the mid-wavelength region, we envision the use of a reduced set of wavelength pairs, choosing those that maximize the sensitivity, specificity and accuracy (i.e., mostly occurring in the mid-wavelength region) and otherwise omitting wavelength pairs that result in poor classification performance. Therefore, the regions with lower accuracy will

not be considered, and the reduced accuracy is not necessarily a limitation of the optimized dual-wavelength atlas method. Instead, the increase of 192 available wavelength pairs with a balanced accuracy $> 95\%$ is considered to provide abundant flexibility when utilizing the optimized dual-wavelength atlas method to differentiate methylene blue from hemoglobin.

The changes in sensitivity, specificity, and balanced accuracy between the LW-SLSC and the chosen GPU-SLSC is explained by the low DSC calculated for the most similar GPU-SLSC mask (i.e., 63.3%). However, the changes in classification performance were not statistically significant, whereas the difference in computation times when switching from LW-SLSC masks to GPU-SLSC masks was statistically significant with a 60.2x speed up factor. Therefore, by using GPU-SLSC for the segmentation of signals of interest, the dual-wavelength atlas method can be further optimized for faster processing times to enable real-time time implementations.

5. CONCLUSION

We optimized a novel acoustic-based atlas method for the differentiation of methylene blue and blood based of an iterative search of six parameters. The optimized version of the dual-wavelength atlas method can detect blood more accurately. In addition, the mean balanced accuracy across multiple wavelength-pair combinations was improved after parameter optimization. This improvement led to an increase in the number of wavelength pairs available to differentiate chromophores of interest with 95% accuracy, offering more flexibility for implementation of our algorithm in clinical practice. Similarly, the use of GPU-SLSC for signal segmentation further optimized the dual-wavelength atlas method for faster processing times, which has the potential to benefit operators of photoacoustic-guided surgery technology that is powered by real-time software.

Acknowledgments

This work was supported by NSF CAREER Award ECCS-1751522, NSF SCH Award IIS-2014088, NSF EEC-1852155, and NIH Trailblazer Award R21-EB025621. The authors acknowledge the support of NVIDIA Corporation with the donation of the Titan Xp GPU used for this research.

REFERENCES

- [1] Wiacek, A., Wang, K. C., Wu, H., and Bell, M. A. L., "Photoacoustic-guided laparoscopic and open hysterectomy procedures demonstrated with human cadavers," *IEEE transactions on medical imaging* (2021).
- [2] Wiacek, A. and Bell, M. A. L., "Photoacoustic-guided surgery from head to toe," *Biomedical Optics Express* **12**(4), 2079–2117 (2021).
- [3] Lediju Bell, M. A., "Photoacoustic imaging for surgical guidance: Principles, applications, and outlook," *Journal of Applied Physics* **128**(6), 060904 (2020).
- [4] Glatz, J., Deliolanis, N. C., Buehler, A., Razansky, D., and Ntziachristos, V., "Blind source unmixing in multi-spectral optoacoustic tomography," *Optics Express* **19**(4), 3175–3184 (2011).
- [5] Tzoumas, S. and Ntziachristos, V., "Spectral unmixing techniques for optoacoustic imaging of tissue pathophysiology," *Philosophical Transactions of the Royal Society A: Mathematical, Physical and Engineering Sciences* **375**(2107), 20170262 (2017).
- [6] Gröhl, J., Kirchner, T., Adler, T., and Maier-Hein, L., "Estimation of blood oxygenation with learned spectral decoloring for quantitative photoacoustic imaging (LSD-qPAI)," *arXiv preprint arXiv:1902.05839* (2019).
- [7] Gröhl, J., Kirchner, T., Adler, T. J., Hacker, L., Holzwarth, N., Hernández-Aguilera, A., Herrera, M. A., Santos, E., Bohndiek, S. E., and Maier-Hein, L., "Learned spectral decoloring enables photoacoustic oximetry," *Scientific reports* **11**(1), 1–12 (2021).
- [8] Mari, J. M., Xia, W., West, S. J., and Desjardins, A. E., "Interventional multispectral photoacoustic imaging with a clinical ultrasound probe for discriminating nerves and tendons: an ex vivo pilot study," *Journal of biomedical optics* **20**(11), 110503 (2015).

- [9] Xia, W., West, S. J., Nikitichev, D. I., Ourselin, S., Beard, P. C., and Desjardins, A. E., “Interventional multispectral photoacoustic imaging with a clinical linear array ultrasound probe for guiding nerve blocks,” in [*Photons Plus Ultrasound: Imaging and Sensing 2016*], **9708**, 97080C, International Society for Optics and Photonics (2016).
- [10] Grasso, V., Holthof, J., and Jose, J., “An automatic unmixing approach to detect tissue chromophores from multispectral photoacoustic imaging,” *Sensors* **20**(11), 3235 (2020).
- [11] Gonzalez, E. A. and Bell, M. A. L., “Acoustic frequency-based differentiation of photoacoustic signals from surgical biomarkers,” in [*2020 IEEE International Ultrasonics Symposium (IUS)*], 1–4, IEEE (2020).
- [12] Gonzalez, E. A., Graham, C. A., and Lediju Bell, M. A., “Acoustic frequency-based approach for identification of photoacoustic surgical biomarkers,” *Frontiers in Photonics* **2** (2021).
- [13] Gonzalez, E. and Bell, M. A. L., “Segmenting bone structures in ultrasound images with locally weighted SLSC (LW-SLSC) beamforming,” in [*2018 IEEE International Ultrasonics Symposium (IUS)*], 1–9, IEEE (2018).
- [14] Gonzalez, E. A. and Bell, M. A. L., “GPU implementation of photoacoustic short-lag spatial coherence imaging for improved image-guided interventions,” *Journal of Biomedical Optics* **25**(7), 1 – 19 (2020).
- [15] Gonzalez, E. A., Jain, A., and Bell, M. A. L., “Combined ultrasound and photoacoustic image guidance of spinal pedicle cannulation demonstrated with intact ex vivo specimens,” *IEEE Transactions on Biomedical Engineering* (2021).
- [16] Guindon, B. and Zhang, Y., “Application of the dice coefficient to accuracy assessment of object-based image classification,” *Canadian Journal of Remote Sensing* **43**(1), 48–61 (2017).
- [17] Kraska-Miller, M., [*Nonparametric statistics for social and behavioral sciences*], CRC Press (2013).